1.5 CCD Subpixel Structure

1.5.1 Introduction and Motivation

The low energy (< 4 keV) quantum efficiency of a front side (FI) CCD is intimately related to the dimensions of the sub-pixel structures. The sub-pixel structures in question include the polysilicon gates and insulating layers, as well as channel stops: implanted p^+ channels and their insulating layers. The gates run the length of the CCD, and are responsible for clocking the charge out of the device. The ACIS CCDs employ a three phase read-out scheme to transfer charge, so the gate structure is actually comprised of three different gates that differ slightly in dimension from one to another [10]. Three neighboring gates define one pixel, with the boundary location dependent on the voltages applied to the gates. Figure 1.43 is an idealized schematic of a CCD cross section revealing the structure of the gates. Figure 1.44 is a SEM cross section of a CCD showing the over lap of gate B with gate A. The rectangular, black regions are the polysilicon gates. The white material over and between the gates is insulating SiO_2.

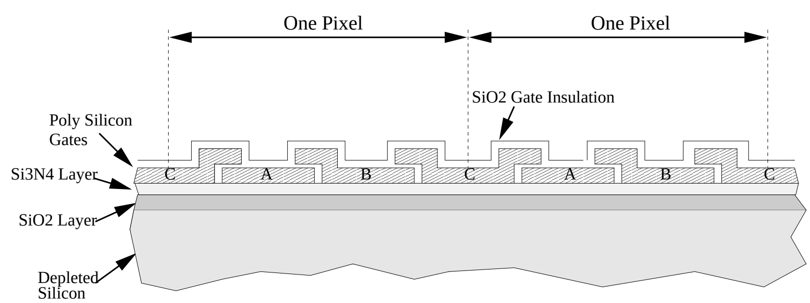

Figure 1.43: Gate structure of a CCD.

The embedded channel stops run perpendicular to and lie beneath the gates. These structures help confine the charge clouds created by a photoelectric absorption and define the horizontal boundaries of a pixel. Figure 1.45 is a picture of a 2×2 array of pixels and shows the orientation of the gates and channel stops to one another. To fabricate the channel stops, a portion of the insulating Si_3N_4 layer is etched away. A p^+ dopant is then implanted into the bulk silicon. Finally, the silicon is oxidized creating an insulating layer of SiO_2 between the channel stop and the gate structure. The gate structure is then grown on top of the silicon after this process. Figure 1.46 is a SEM measurement of a channel stop. The black and white bands at the top of the image are the polysilicon gates and insulating oxide, respectively. The elongated, hexagonal structure is the SiO_2 insulator between the

p^+ channel (not visible in this image) and the gates. The thin white structure between the gates and hexagonal insulator is the Si_3N_4.

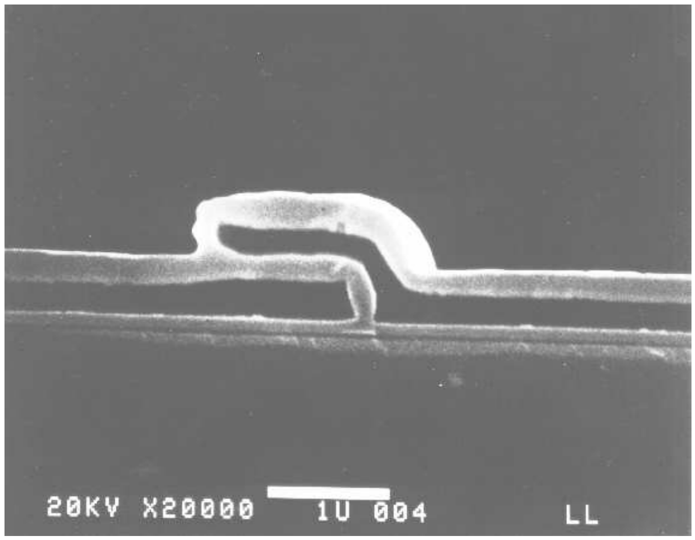

Figure 1.44: SEM photo of the CCD gate structure. Gate B is shown overlapping gate A. The bar above the text in the photo is 1 μm.

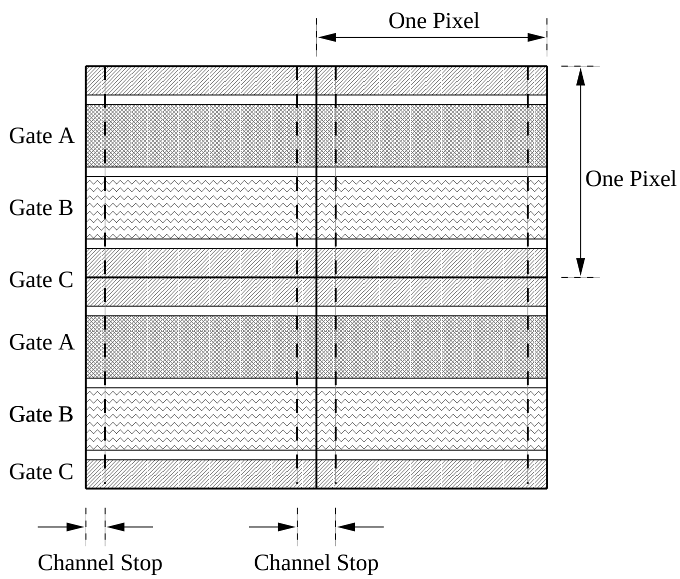

Figure 1.45: Schematic of a 2×2 array of pixels showing the orientation of the gates and channel stops. The channel stops are beneath the gates.

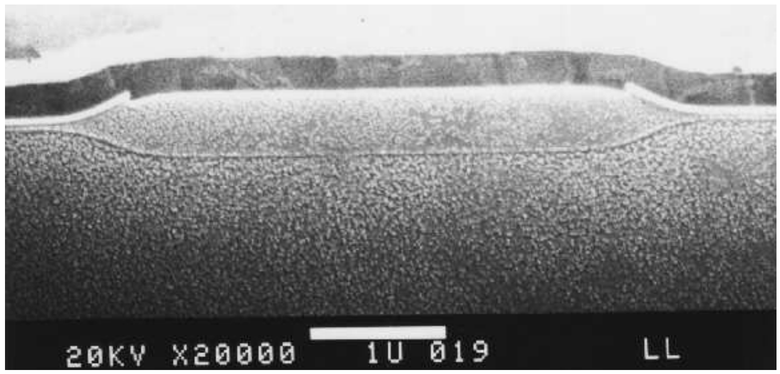

Figure 1.46: SEM measurement of a channel stop

When modeling the quantum efficiency of an ACIS CCD, the complicated gate structure can accurately be approximated as uniform slabs of material that cover the entire CCD. This model assumes that the charge created by a photon interaction in one of these layers is not collected by the device (i.e. the layer is "dead"). This model–The Slab and Stop model–was first developed by Keith Gendreau during calibration of the ASCA SIS CCDs [14]. The Stop part of the model refers to treating the hexagonal insulator structure and implanted p^+ as rectangular regions of dead SiO_2 and Si, respectively. The absolute calibration of the reference standards involves fitting the data obtained at the BESSY facility with the Slab and Stop Model. While the BESSY measurements determine the thicknesses of the gate slabs, they prove insufficient for constraining the channel stop parameters[1]. Construction of a highly accurate CCD model, then, requires determination of this information in some other fashion.

1.5.2 Description of Mesh Experiments

One possible method for determining the sub-pixel structure is illuminating a pixel with a very narrow beam of monochromatic X-ray and observing how the CCD response changes as the beam is rastered across the pixel. Unfortunately, obtaining a well focused X-ray beam is difficult, and even if it were trivial, the experiment would require too much time to acquire enough data to make the results statistically significant. One possible solution to both of these problems is using a metal film with relatively small holes (4 μm holes compared to the 24 μm size of a pixel) placed in a regular fashion [13]. When this mesh is placed close to the CCD surface and rotated with respect to the axes defined by the gate

[1]See Section 1.6.1 for details.

structure and channel stops, a moiré pattern is formed when the device/mesh combination is illuminated with X-rays. Below, we summarize the experimental technique and our initial results. Interested readers are referred to the paper by Pivovaroff *et al.* for details [27].

Figure 1.47 shows a section of the mesh, and Figure 1.48 shows the fixture used to hold the mesh tight and close to the surface of the CCD. The resulting moiré pattern contains the CCD's response to a 4 μm X-ray beam that was uniformly rastered across the pixel area. The smaller the relative angle between the mesh's orientation and the CCD axes, the more pixels are required to make a moiré cell, and the finer resolution of the CCD's response[2]. Typical measurements were performed with angles on order of 5°, and moiré cell dimensions of 61 pixels.

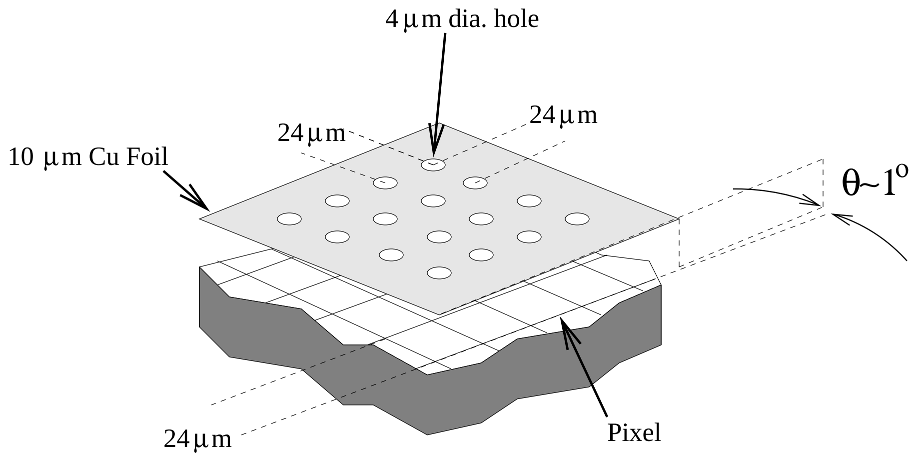

Figure 1.47: Schematic of the mesh showing its orientation to the CCD

Analysis of the data begins with selecting suitable grade events (single pixel and horizontally or vertically split events) from the photo-peak of the monochromatic line to build the moiré cells, rotating the moiré cells, and summing individual cells into one representative pixel (hereafter RP) for the entire CCD. Figure 1.49 shows a sample of the unrotated, raw moiré cells that are a direct output of the illumination of the mesh/CCD system and the RP, repeated in a 3×3 array to make it easy to see the boundary regions of the pixel. With the RP generated, determination of the sub-pixel structure can proceed. By compressing the RP in one direction, the attenuating affect of the channel stops or the gates can be modeled. For the rest of this review, we concentrate only on the channel stops, although the same techniques can be applied to measure the gates.

[2] Readers are referred to the paper by Tsunemi [13] for the analytic derivation of these relationships.

The approach for determining the channel stop dimensions is quite straightforward. The attenuation in detected photons expected from the channel stop (recall that the Slab and Stop Model assumes that any photon interacting in the sub-pixel structure will not be detected) is convolved with the PSF of the mesh holes. The resultant convolution is compared to the experimental data, and the channel stop model parameters are allowed to vary, using a χ^2 fit statistic to determine the best-fit parameters. Figure 1.50 shows the five parameters used to describe the channel stop. Compare the model to the SEM photo of an actual channel stop in Figure 1.46.

In addition to constructing a realistic channel stop model, the success of this technique depends on providing an accurate PSF for the mesh and accounting for additional processes that effectively broadens the PSF (i.e. diffraction, diffusion of the charge cloud, distortions to the PSF caused by using a non-parallel X-ray source). Producing such an analytic aperture function (hereafter AF) is a daunting task. Fortunately, the AF can be ascertained from the mesh data itself. Horizontal and vertical split events come from photons that interact within an electron cloud size diameter of the pixel boundary. Analysis of BESSY KMC data performed by Jones and Prigozhin [28] indicate that cloud sizes range between 10 and 100 nm. The distribution of the horizontal and vertical split events ($\Delta_{split\ events}$), then, is the convolution of a 10-100 nm step function (Θ) with the AF.

$$AF \otimes \Theta = \Delta_{split\ events} \tag{1.18}$$

The projection of the mesh holes on the surface of the CCD are at least 4.5 μm in diameter, so Θ can be approximated as a δ function. Equation 1.18 then becomes

$$AF \otimes \Theta \approx AF \otimes \delta = AF = \Delta_{split\ events} \tag{1.19}$$

1.5.3 First Results

Two different X-ray sources were used to perform measurements at six different energies. A monochromator produced photons corresponding to the O Kα line, and the HEXS electron impact source [7] produced Al, Si, P, Cl and K Kα lines. Table 1.23 shows the number of photons collected at each of the energies. Figure 1.51 shows the relative amount of attenuation caused by the channel stops, modulated with the mesh AF. The amount of attenuation is governed entirely by the characteristic attenuation lengths of the Kα photons in Si, SiO_2, and Si_3N_4 and does not simply monotonically decrease with increasing photon energy.

Fitting the channel stop model to data from only one Kα line results in degeneracies in the model. Effectively, the five parameters reduce to two: the total width of the stop and the total attenuation. These are given by:

$$\mathrm{Width}_{Total} = 2 \times \mathrm{Width}_{wing} + \mathrm{Width}_{box}$$
$$\mathrm{Atten}_{Total} = \mathrm{Atten}_{Si} \times \mathrm{Atten}_{SiO_2} \times \mathrm{Atten}_{Si_3N_4}$$

The upper two panels of figure 1.52 show the χ^2 confidence plots for the O Kα data set and the P Kα data sets. The contours are for the 68%, 90% and 99% confidence levels. The box and wing parameters have great uncertainty, but the constant slope of the contours does indicate some bound to the total width. The situation is similar for the thicknesses of the Si p^+ channel and the insulating SiO_2. By simultaneous fitting multiple data sets, a tighter constraint can be placed on the model. The bottom panels of figure 1.52 show the χ^2 contours for the five HEXS data sets (Al,Si,P,Cl, and K). Taken together, these data still do not tightly constrain the width parameters, but do provide estimations for thicknesses of the p^+ and SiO_2. Table 1.24 lists the parameter, the range of parameter space and grid sized used, and the derived best fit-value (90% confidence levels) from the simultaneous fitting.
Unfortunately, the O Kα χ^2 contours do not overlap the the HEXS data χ^2 contours. Figure 1.53 shows the experimental data and the model with the best-fit values derived from combining all five HEXS measurements. The difference between the oxygen data and the model is quite severe, and no set of acceptable HEXS parameters yield a reasonable fit to the oxygen data. A number of possibilities have been explored to explain the discrepancy. The oxygen data was obtained with a different X-ray/vacuum system than the HEXS data and scattering may have been present. Scattering would have the effect of introducing a false background to the system and thus influence the measure of relative attenuation. The monochromator data also had a steep position dependent intensity gradient. In order to add the moiré cell data to produce the RP, a correction had to be applied to the raw data to normalize the flux across the CCD imaging area. This correction also could have introduced an error into the data.

In addition to the suspected problems with O Kα data, there is a disagreement between the best-fit parameters and other, independent measures of the channel stop dimensions. The manufacturers of the CCDs, MIT Lincoln Laboratories, reports that about one μm of p^+ dopant is implanted to make the channels, not 0.35 μm as determined by the mesh experiments. Many SEM measurements were performed on chips identical to the CCDs. These photos, exactly like Figure 1.46, show that the SiO_2 thickness is about 0.45 μm, not 0.70 μm. The same SEM studies, however, do show that the box and wing parameters obtained by the mesh studies agree with physical reality.

The discrepancy between the dimensions obtained from the experiments and those known either from the fabrication process or from direct measurement indicate flaws in the experimental technique or an incorrect model. As part of our attempt to understand our results, we have begun a series of new investigations that show great promise in explaining the inconsistencies. The key refinement to the experimental technique is the use of a mesh with square holes $\sim$1.4μm on a side. The smaller hole size allows the sub-pixel structure to be probed with significantly greater detail. Figure 1.54 shows g0 event pixel maps at O Kα (525 eV) made with the 4μm mesh and the new, 1.4μm mesh. The marked improvement in resolution offers the possibility of not only increasing the accuracy of the channel stop parameters, but also studying the small scale structures in the gates (i.e. gate overlaps). See Section 1.14 for the model predictions.

There also exists the distinct possibility that the Slab-and-Stop model is too simplistic and does not properly account for all the physical processes occurring inside the device. In fact, we have recently achieved a significant breakthrough in our understanding of the charge loss mechanism. We are currently exploring the details of these processes and will report on these results once our investigations are complete.

1.5.4 Prospects for sub-pixel resolution

In addition to revealing the dimensions of sub-pixel structures, the mesh experiments also hint at the possibility of improving the spatial resolution of the CCD beyond that of a 24 μm pixel device. Before continuing, a short digression on event grades is necessary. The CCD registers an event when the charge cloud created by a photoelectric absorption is pulled into the potential of one of the gates. Some fraction of the time, the charge is divided into multiple pixels. Theoretically, this fraction, the branching ratio, depends on what depth in the silicon the interaction took place and where it occurs with respect to the pixel boundaries. According to this scheme, single pixel events (ASCA grade 0) come from photons that land in the center of the pixel, vertically split events (ASCA grade 2) come from photons that land near the vertical boundary of the two pixels, horizontally split events (ASCA grades 3 and 4) come from photons that land near the horizontal boundary of two pixels, and three and four pixel events (ASCA grade 6) come from photons that land in the corner of a pixel. The mesh experiments, for the first time, have conclusively proven that this simple picture is in fact correct. Figure 1.55 shows the 3×3 RP arrays from the O Kα data for grade 0, grade 2, grade 3 and 4, and grade 6 events. It is obvious that the horizontal and vertical split events come from the boundary regions and that the multiple pixel events come from the corner regions. At the same time, the single pixel RP events occur only in the center of the pixel.

The confinement of certain event grades to a specific area of the CCD is effectively like having smaller pixels inside a 24 μm pixel and is the key to obtaining sub-pixel resolution. The branching ratios are a strong function of energy and penetration of the photon into the device. As the percentage of multiple pixel events increase, these mini-pixels will increase in size. Figure 1.56 shows two 3×3 pixel grids. Both grids show a geometric area (computed from the branching ratios) for the different event grades discussed above, one for Si Kα photons (1.740 keV) and one for Cu Kα photons (8.040 keV). Superimposed on each of these grids are the 33% and 66% enclosed energy curves for the HRMA. A full, mathematical investigation has not been performed, but the hope is that by comparing the branching ratios from an astronomical observation with ground calibration data, the source location can be determined to better than one pixel.

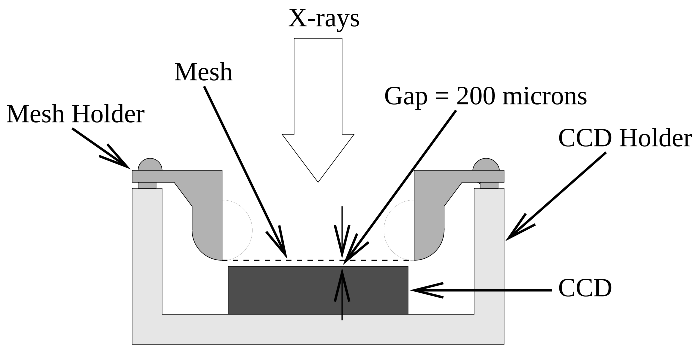

Figure 1.48: Fixture used to hold the mesh close to the CCD surface

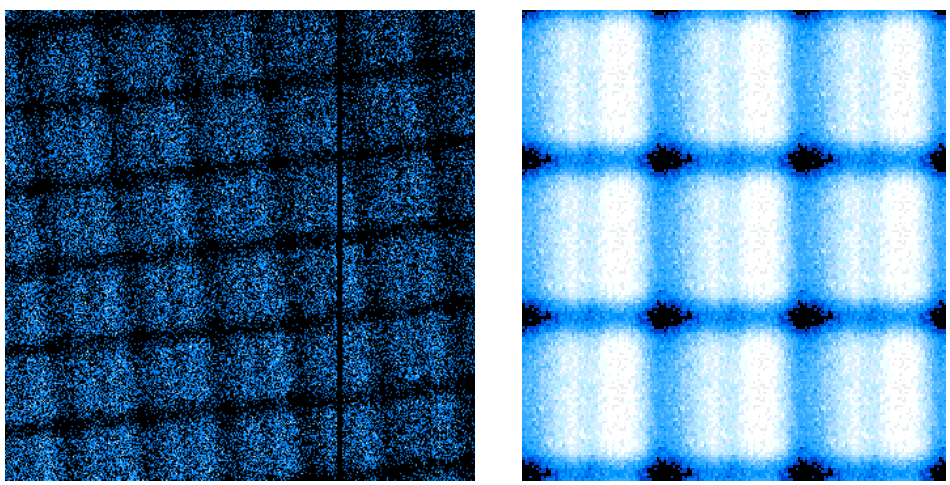

Figure 1.49: Left: Raw data showing the moiré cells. Right: The representative pixel (RP) repeated in a 3×3 array.

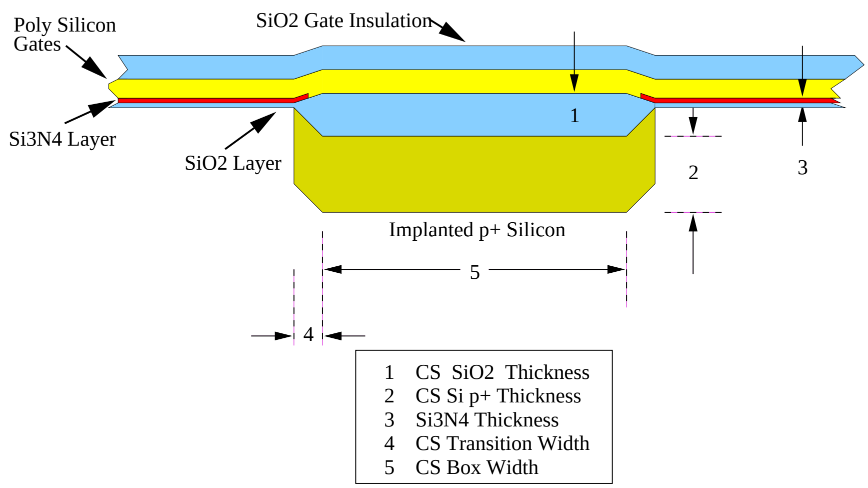

Figure 1.50: Five parameter channel stop model.

K_α	Energy (eV)	total counts
O	525	4.5×10^5
Al	1487	8.4×10^4
Si	1740	6.8×10^4
P	2035	2.2×10^5
Cl	2622	5.5×10^4
K	3312	7.7×10^4

Table 1.23: Summary of Mesh Measurements

parameter	parameter space data		best fit-value
	search range	step size	
box width	3.1-4.5 μm	0.16 μm	$4.2^{+.3}_{-.4}$ μm
wing width	0.12-1.2 μm	0.12 μm	$.35^{+.19}_{-.12}$ μm
Si thickness	0.12-1.2 μm	0.12 μm	$.35^{+.06}_{-.03}$ μm
SiO_2 thickness	0.12-1.2 μm	0.12 μm	$.71^{+.17}_{-.11}$ μm
Si_3N_4 thickness	0.0-0.05 μm	0.01 μm	insensitive

Table 1.24: Information from Simultaneous Fitting to all Five HEXS Data Sets

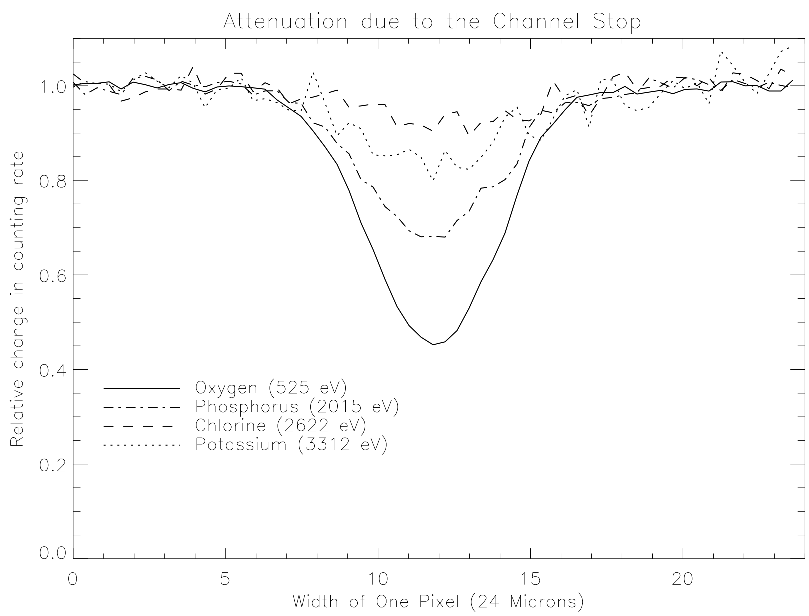

Figure 1.51: Variation in detection efficiency due to the channel stop

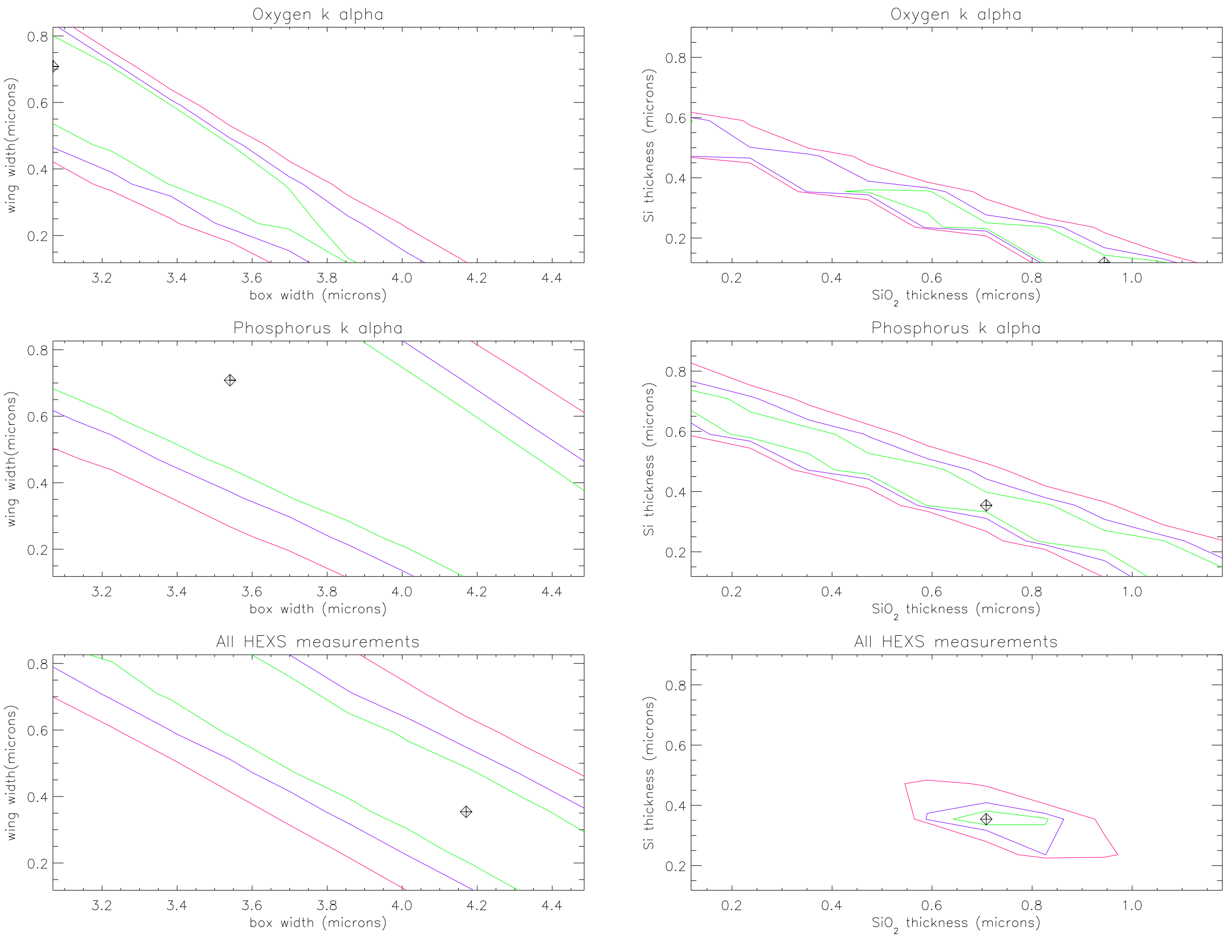

Figure 1.52: χ^2 contour plots for box width vs. wing width and Si p^+ depth vs. SiO_2 depth. Contours are the 68%, 90%, and 99% confidence levels.

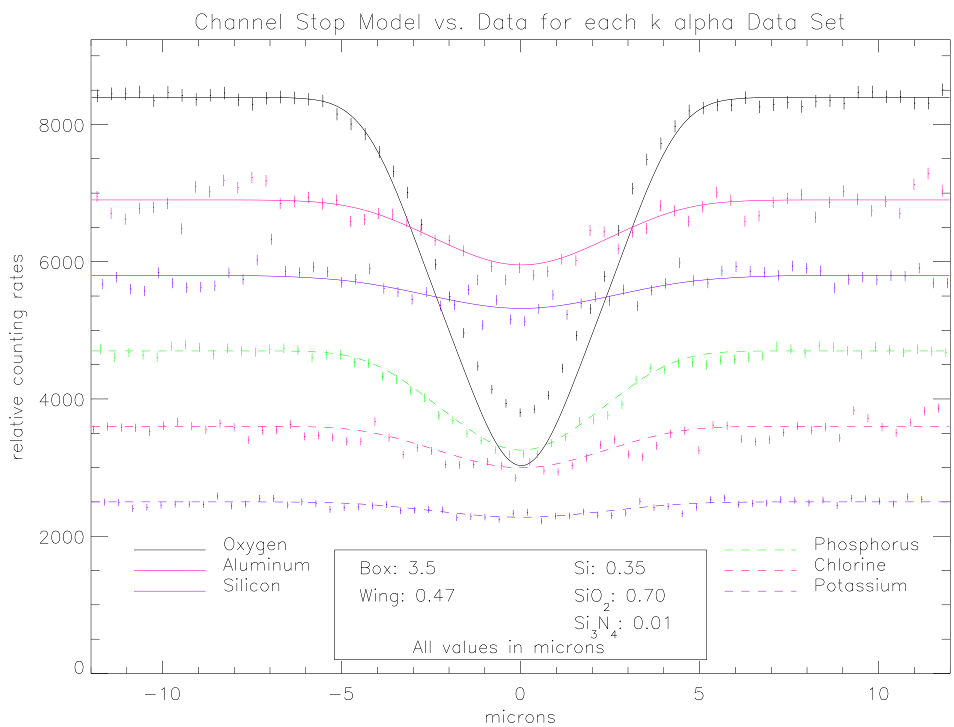

Figure 1.53: Best-fit HEXS channel stop model compared to experimental data.

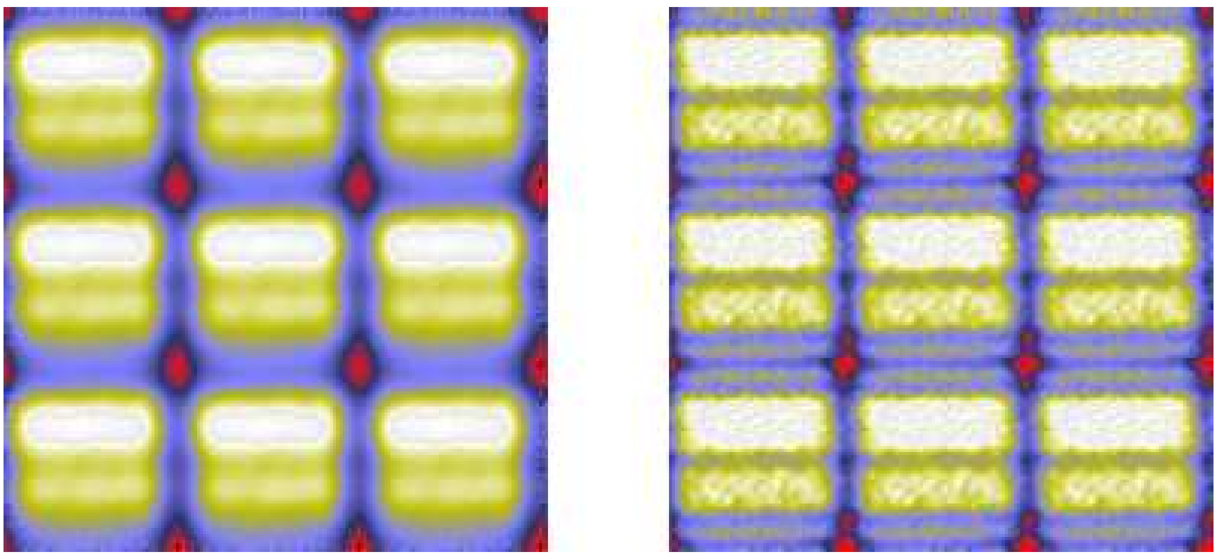

Figure 1.54: Intensity of grade 0 events at O Kα. **Left:** Results from the 4μm mesh. **Right:** Results from the 1.4μm mesh. Data has been smoothed with a boxcar function approximating the mesh aperture. The new mesh provides significant resolution of the sub-pixel structures.

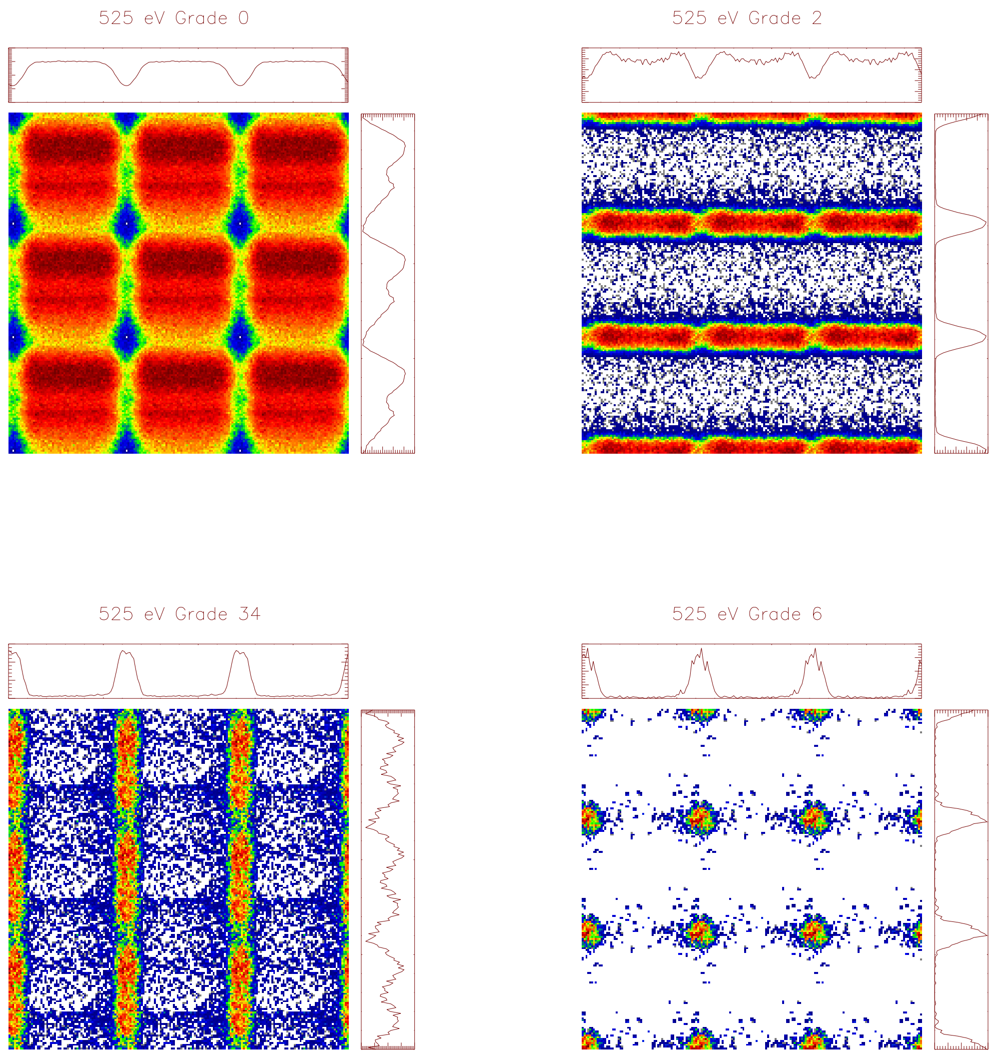

Figure 1.55: O Kα Representative Pixels for grade 0, grade 2, grades 3 and 4, and grade 6events.

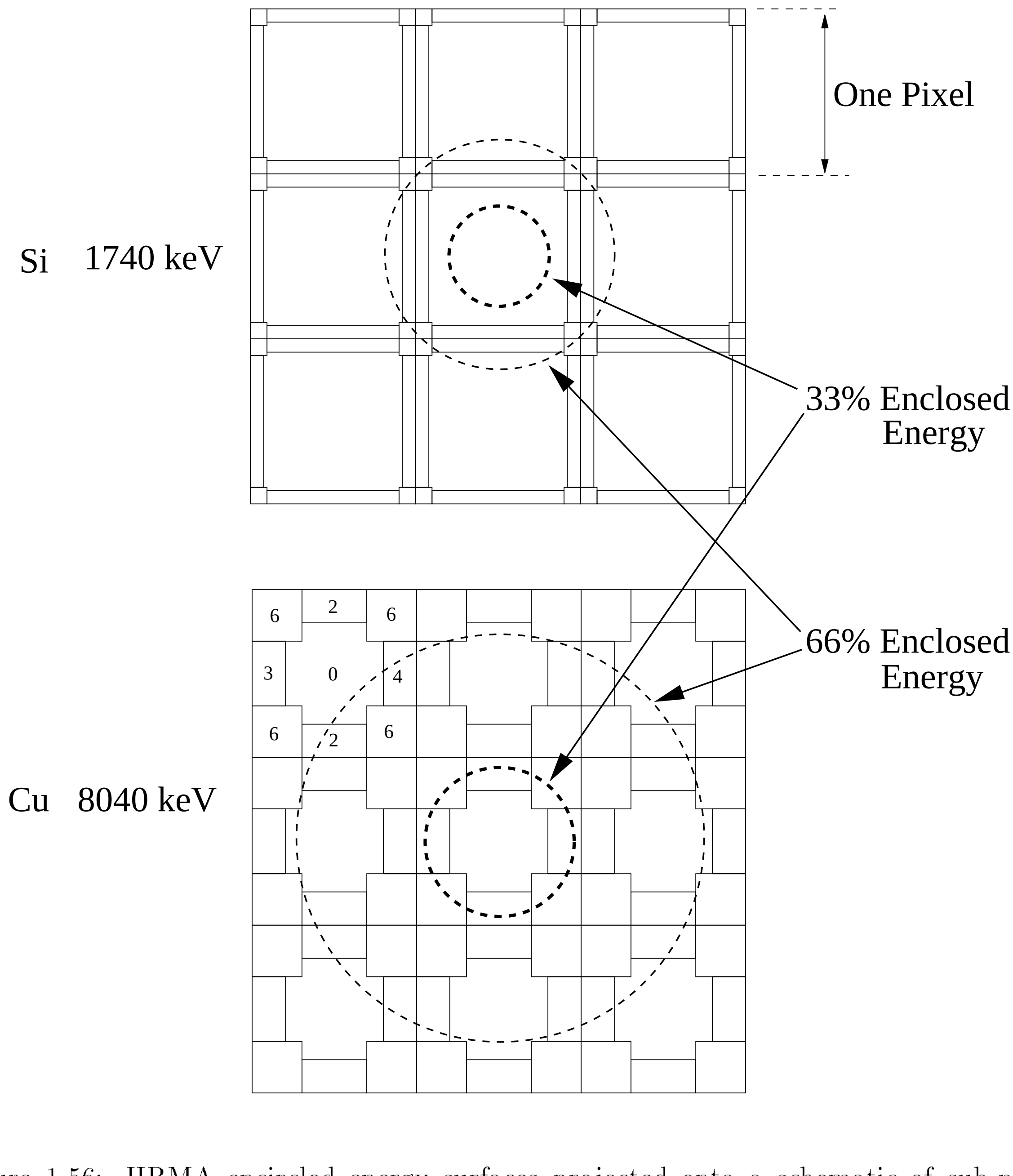

Figure 1.56: HRMA encircled energy surfaces projected onto a schematic of sub-pixel locations